DOI: 10.1002/adfm.200902089

Control of solid-state dye-sensitized solar cell performance by block copolymer directed TiO_2 synthesis

By *Pablo Docampo*,[†] *Stefan Guldin*,[†] *Morgan Stefik*, *Priti Tiwana*, *M. Christopher Orilall*, *Sven Hüttner*, *Hiroaki Sai, Ulrich Wiesner*, *Ulrich Steiner*,[*] and *Henry J. Snaith**

[*] Dr. Henry J. Snaith, Mr. Pablo Docampo, Mrs. Priti Tiwana
Department of Physics
Clarendon Laboratory
University of Oxford, UK OX1 3PU;
E-mail: h.snaith1@physics.ox.ac.uk

Prof. Ulrich Steiner, Mr. Stefan Guldin, Mr. Sven Hüttner
Department of Physics
Cavendish Laboratories
University of Cambridge, Cambridge, UK CB3 OHE
E-mail: u.steiner@phy.cam.ac.uk

Prof. Ulrich Steiner,
Freiburg Institute for Advanced Studies (FRIAS)
Abert-Ludwigs-Universität Freiburg
Albertstraße 19, D-79104 Freiburg, Germany

Prof. Ulrich Wiesner, Mr. Morgan Stefik, Dr. M. Christopher Orilall, Mr. Hiroaki Sai
Department of Materials Science & Engineering, Cornell University, Ithaca, New York 14853, USA

Keywords: self-assembly, block copolymer, sol-gel, efficiency, dye-sensitized solar cell, solid-state

Hybrid dye-sensitized solar cells are typically composed of mesoporous titania (TiO_2), light harvesting dyes and organic molecular hole-transporters. Correctly matching the electronic properties of the materials is critical to ensure efficient device operation. In this study we synthesize TiO_2 in a well defined morphological confinement that arises from the self-assembly of a diblock copolymer - poly(isoprene-*b*-ethylene oxide) (PI-*b*-PEO). We show that the crystallization environment, tuned by the inorganic (TiO_2 mass) to organic (polymer) ratio, is a decisive factor in determining the distribution of sub band gap electronic states and the associated electronic function in solid-state dye-sensitized solar cells. Interestingly, the tuning of the sub band gap states does not appear

to strongly influence the charge transport and recombination in the devices. However, increasing the depth and breadth of the density of sub band gap states correlates well with an increase in photocurrent generation, suggesting that a high density of these sub band gap states is critical for efficient photo-induced electron transfer and charge separation.

1. Introduction

Nanostructured composites have become increasingly attractive for their exciting, and in some instances unexpected, properties compared to their bulk characteristics.[1] A wide range of applications are being developed in diverse areas,[2] such as catalysts,[3] light-emitting diodes,[4] biosensors,[5,6] and photovoltaic devices.[7] There has been a huge effort in the development of different routes to obtain these nanostructured materials, from simple colloidal synthesis[8] to more elaborate structures with regular nanopores such as those obtained from liquid crystal templating of inorganic materials.[9]

More recently, nanostructured materials have been prepared through the self-assembly of block copolymers which microphase separate into highly ordered morphologies including spherical, cylindrical, lamellar and gyroidal domains. The tunability of shape and length-scale gives unparalleled control over the resulting self-assembled structures and offers a powerful tool for nanotechnology.[10] Some strategies involve creating templates from these soft materials. Typically, one block is selectively removed while the other one is used as a scaffold allowing the backfilling of complex structures, such as the gyroid phase.[11,12] Another approach for the synthesis of nanocomposites involves the selective incorporation of inorganic sol into a single block of an amphiphilic block copolymer. Pioneered by Templin *et al* in 1997,[13] access to predicted diblock copolymer phases has been achieved through the selective swelling of aluminosilicate sol into the PEO phase of a block copolymer. Later, Stucky *et al*.[14,15] incorporated metal–oxide sols into an ABA triblock copolymer (poly(ethylene oxide-*b*-propylene oxide-*b*-ethylene

oxide), Pluronics P123). The resulting transition metal oxide containing nanocomposites were subsequently heat treated in air to calcine the metal oxide while oxidatively removing the polymer, producing an ordered mesoporous amorphous or partly crystalline framework. The use of P123 typically limits the pore size to between 6 and 14 nm, which is too small for some applications, and may impede the complete crystallization while maintaining structural integrity.[16] An alternative copolymer to use as a structure directing agent is poly(isoprene-block-ethylene oxide) (PI-*b*-PEO). This block copolymer offers several advantages such as the insitu formation of a carbon scaffold at high annealing temperatures in inert atmosphere, enabling the complete crystallisation of metal oxides like Nb_2O_5 or TiO_2 without loss of the mesostructure.[17] Furthermore, pore sizes ranging from 20 to 80 nm[18] have been achieved by varying the molecular weight of the polymer. As a consequence of the high interaction parameter between the two building blocks, PI and PEO, and the low glass transition temperature, highly regular block copolymer morphologies such as hexagonal cylinders, lamellae, gyroid, and plumber's nightmare morphologies have been shown for aluminosilicate.[13,17,19]

A technologically interesting application for these mesoporous crystalline materials is the dye-sensitized solar cell (DSC), introduced in its current form by O'Reagan and Grätzel in 1991.[20] Dye molecules sensitize the surface of mesostructured metal oxides such as TiO_2. Photo-induced electron transfer occurs from the photo-excited dye into the conduction band of the TiO_2. The electrons are then free to percolate through the interconnected TiO_2 nanoparticles to be collected at a transparent conducting anode on the underside of the film. The circuit is completed through the regeneration of the dye by an iodide/triiodide redox couple in form of an electrolyte which carries the hole species to the cathode. In order to avoid reported problems with solvent leakage and corrosion of liquid electrolytes, [21] Bach *et al.* [22] replaced the electrolyte with a molecular organic

hole transporter, spiro-OMeTAD in 1998. With this solid-state concept, power conversion efficiencies of up to 5% have been achieved.[23] Despite its conceptual advantage, there are considerably more technical and subtle issues involved in creating an ideal solid-solid nanocomposite, rather than the solid-liquid composite of the original DSC. A critical step is the infiltration of the mesoporous titania network with a molecular hole transporter, which is influenced by the structure of the underlying oxide. Moving from a system with strong charge shielding by an electrolyte to a system where 50% of the composite has a dielectric constant as low as 3 has a significant influence on the electronic processes of charge generation, separation, transport and recombination. The control of the underlying properties of the metal-oxide film such as structure, crystallinity, surface area[24] and nature of electronic states is therefore crucial for device optimization.[25]

Previously, we have applied self-assembled block copolymer morphologies to the solid-state DSC: For one route, films were fabricated by spin-coating a titania sol containing diblock copolymer solution directly on the device substrate with subsequent annealing and semicrystalline mesoporous film formation.[18] The second route involved replicating the double gyroid phase into titania by electro-deposition through a nanoporous block copolymer generated template.[11,12] Both of these routes delivered very encouraging results, and demonstrate the range of structures achievable through block copolymer self-assembly and replication into active semiconductor devices. However, they both suffer from difficulties in making the films suitably thick, since the crystallization process occurs on the device substrate. A volume contraction during calcination induces in-plane strain which leads to the formation of cracks in thick sintered films. Recently we have presented an alternative approach where we decouple the material calcination process from the actual film fabrication[26]. In this case, monolithic crystalline TiO_2 is ground

down and processed into a paste to coat the substrates, forming crack-free, albeit rough, films up to many micrometers in thickness.

Here, we apply these processable mesoporous films to solid-state dye-sensitized solar cells, and reveal another key characteristic of block-copolymer derived mesoporous TiO_2. According to our findings, block copolymers do not only play an important role for morphological aspects but also decisively influence the crystallization and associated electronic properties of TiO_2. We have studied the influence of changing the composition of the metal oxide synthesis, on the electronic nature of the ensuing mesoporous TiO_2, and demonstrate that subtle changes to the crystallization landscape have an extensive influence on the electronic solar cell functionality.

2. Results and discussion

2.1. Control of the titania mesostructure through PI-*b*-PEO self-assembly

Solid-state DSC devices were manufactured from mesoporous TiO_2 layers in the following fashion (see experimental section for details). A PI-*b*-PEO block copolymer with a molecular weight M_n = 33.5 kg mol^{-1}, polydispersity 1.03 and a PEO weight fraction of 0.23 was dissolved in anhydrous tetrahydrofuran (THF). Ti-ethoxide in HCl was added. Following the evaporation of the solvent, the material was calcined to anatase TiO_2 at 500 °C in air. The resulting mesoporous monolith was briefly ground to a powder (60 seconds) and processed into a paste by solvent and cellulose addition following a similar method to Ito *et al.*[27] albeit with only one minute grinding and brief ultrasonification. To investigate the influence of the crystallization environment on the solar cell performance, titania hybrid composites were synthesised using three different precursor to block copolymer ratios. The mixing ratios of the sol to polymer solutions

were adjusted in such a way that the weight of the TiO_2 after calcination as compared to the weight of the polymer in the solution had the ratios 1:3, 1:1 and 2:1. Titania derived from the three different recipes is referred to as “titania 1:3”, “titana 1:1”, and “titania 2:1” in the reminder of the article. **Figure 1a** is a schematic illustration of the sol gel self assembly process, and **Figure 1b-d** are schematics of the block copolymer directed morphologies for titania 1:3, 1:1 and 2:1 respectively.

In **Figure 1e**, **1f**, and **1g** we present TEM images of the bulk hybrid material before calcination. The 1:3 recipe yielded an array of amorphous titania cylinders surrounded by a matrix of PI. Cylinders with a differing alignment with respect to the image plane are discernible in Figure 1e. The 1:1 recipe (Figure 1f) resulted in an inverse micellar morphology containing PI spheres surrounded by a matrix containing both PEO and amorphous titania. Although, a lamellar morphology was expected for the 1:1 ratio,[28-30] we suspect that the use of roughly equal portions of two selective solvents induced micellization of the polymer which resulted in toluene and PI rich micelles surrounded by a matrix rich in butanol, PEO and titania. Such a solvent induced morphology[31] could become kinetically trapped by titania condensation during the casting process resulting in an inverse micellar morphology. Finally for the 2:1 recipe in Figure 1g, an inverted morphology of an amorphous titania phase has formed around a well ordered array of PI cylinders. Small angle X-ray scattering (SAXS) patterns are consistent with the above findings (see Supporting Information). **Figures 1h, 1i, 1j** show the calcined materials after heat treatment in air at 500ºC. The titania 1:3 sample has predominantly collapsed since there is no self supporting scaffold once the polymer is removed, though elongated features with a cylinder-like morphology can still be seen. Samples with a higher inorganic ratio (titania 1:1 and 2:1) maintained their previous morphology.

Powder X-ray diffraction was employed to probe the crystal polymorph and size in the resulting films processed from pastes. Initially, after calcination of the monolith at 500°C for 2 hours, the crystal phase was entirely anatase consisting of nanocrystals with sizes of 10.1 ± 0.2 nm for the 1:3 ratio, 11.2 ± 0.1 nm for the 1:1 ratio and 12.7 ± 0.1 nm for the 2:1 ratio as determined by Debye-Scherer peak width analysis of the anatase (101) peak. After grinding, sonication, paste formation and resintering of the film at 500 ºC on the substrate, the crystallites were similar for the three compositions, with sizes of 13.9 ± 0.3 nm, 13.3 ± 0.3 nm and 14.1 ± 0.3 nm for titania 1:3, 1:1 and 2:1, respectively (see supplementary information for XRD spectra). While the size of the nanocrystals varied for the three recipes after the first calcination step, a less significant trend is discernible upon re-sintering the paste, and similar final sizes are reached for all three initial compositions. The SEM images in **Figure 2**, (d) to (f) depict the final mesoscopic film morphology of all the ratios and it is evident that all morphologies are similar after grinding, sonification, paste formation and subsequent annealing. Additionally, the Brunauer-Emmett-Teller (BET) specific surface area obtained from nitrogen physisorption of the film processed materials are very similar for the three initial TiO_2 to polymer ratios, ~60 m^2g^{-1} (data not shown), while any added porosity during paste processing of the films was kept constant by the addition of ethyl-cellulose in a 1:2 (cellulose:TiO_2) ratio by weight. It is important to emphasize that the initial block copolymer-derived morphologies of Figure 1 are predominantly lost during the grinding process utilized for device manufacture: The titania layers in the three device cross-sections, shown in Figure 2, are indistinguishable in terms of porosity, TiO_2 morphology and crystallinity. Although this limits the control of the mesostructure in these "processable" films, the three types of titania have a different preparation history. This provides us with an excellent framework to study the electronic properties of mesoporous materials that were synthesised from different (but controlled) initial conditions, while

keeping factors such as surface area, crystal size, dye uptake, light scattering, and hole transporter infiltration relatively constant.

2.2 Solar cell performance and electronic characteristics

Solid-state dye-sensitized solar cells were fabricated by staining the mesoporous electrodes with a dye-sensitizer, termed D102, and filling the dyed electrodes with 2,2',7,7'-tetrakis(N,N-di-*p*-methoxyphenylamine)-9,9'-spirobifluorene (spiro-OMeTAD) via spin-coating. Final electronic contact was made by capping the devices with silver electrodes. After filling the pores, the hole transporter has to create a thin and uniform capping layer on top of the electrode to introduce the necessary electronic asymmetry of the device, establishing a selective contact of the organic hole conductor with the metal electrode. On the other hand, a thick capping layer increases the series resistance in the device and limits the fill factor.[32] The herein created films were extremely rough, and, following the standard coating protocol (15 wt% spiro-OMeTAD in chlorobenzene spin-coated at 2000 rpm)[33] only relatively poor device performances were obtained.

The degree of pore filling and the thickness of the capping layers are important factors influencing the device performance. This requires a careful investigation of the spiro-OMeTAD processing step that can be finely tuned by varying the concentration of the casting solution and the spin-coating speed. [33,34] We varied the thickness of the mesoporous layers and the concentration of the spiro-OMeTAD casting solution. In **Figure 3a-3d** the solar cell performance parameters are shown for devices incorporating titania 2:1 paste electrodes of a range of different thicknesses. The performance parameters are plotted against spiro-OMeTAD concentration in the starting solution, measured under 100 mWcm^{-2} AM 1.5 simulated sun light. The basic observation is that devices between 1 to 3 microns in thickness operate reasonably well with casting

solutions containing between 20 to 30% spiro-OMeTAD (c.f. 15% for standard devices, i.e. fabricated from commercially available nanoparticle pastes). The evolution of the solar cell performance parameters with spiro-OMeTAD concentration is a convolution of the increasing film thickness, pore filling and capping layer thickness.[33,34] For the thin films (up to 0.5 μm), the layer roughness is comparable to the overall film thickness, making it challenging to form an optimum composite. **Figure 3a** shows the fill factor as a function of spiro-OMeTAD concentration, with the film thicknesses noted in the legend. At low spiro-OMeTAD concentrations the pore filling improves with increasing concentration resulting in an increase in fill factor. The solubility limit for spiro-OMeTAD in chlorobenzene is close to 35 % and hence the use of high concentration solutions does not improve pore filling, but increases the thickness of the capping layer causing a lower fill factor. Too thick capping layers appear to limit the device performance by increased resistive losses, though we note that pore filling may also be inhibited by excessive concentrations of the casting solution. The optimum combination of parameters is a TiO_2 film thickness of 1.6 μm and a spiro-OMeTAD solution concentration of 25%. This is a considerably higher concentration than the optimised concentration of 15% required for devices manufactured from smooth films made with standard TiO_2 nanoparticles. This is probably due to the requirement of having a considerably thicker spiro-OMeTAD capping layer to completely cover the rough undulating film.

To illustrate the roughness of the layers and the apparent difficulty of uniformly filling and capping these “undulating” films, a cross sectional SEM image of a solid-state DSC incorporating a titania 1:3 film is shown in **Figure 3e**. Even though this is one of the roughest devices of the series, the device delivered a power conversion efficiency of over 3%. In contrast to our previous assumptions, this clearly demonstrates that the solid-state

DSC is compatible with rough non-uniform films. Upon close inspection of the SEM image, it is apparent that both the spiro-OMeTAD capping layer (darker region near the top), and the silver electrode (bright capping material) are to a greater or lesser degree conforming to the undulating surface. This is a likely explanation for the good fill factor of these devices. A similar study of film thickness and pore filling as shown for titania 2:1 in **Figure 3** was conducted for the remaining two titania ratios, and the best performing cells from each series are characterized electronically in more depth below. The roughness of the films is a consequence of the employed fabrication pathway to mesoporous TiO_2 films. In an earlier publication we showed that in the presented fabrication approach the basic constituents, titania nanocrystallites, typically agglomerate into building blocks on the micrometer length scale, which has the fortunate effect of uniting scattering and a high surface area for dye loading and ensuing light harvesting in a single, thin layer[26].

Figure 4-a shows the normalized photovoltaic action spectra for the optimized devices based on pastes made with all three titania recipes as well as the normalized incident photon-to-electron conversion efficiency (IPCE) for a device fabricated from standard TiO_2 nanoparticle paste for comparison (we have normalized the curves to compare the shape), all cells are sensitized with the same dye, D102. As mentioned previously, the mesoporous material fabricated from all three titania recipes have similar surface areas, and judging by the normalized IPCE spectra, they have similar light absorption profiles. As compared to the reference standard nanoparticle based device, the block copolymer spectra are narrower, suggesting a slightly lower absorption depth in the block copolymer derived composites. A study of the variation of photovoltaic action spectra with the cell thickness was also performed and is shown in supporting information 3. The width of the action spectra increases monotonically with increasing film thickness. The “standard nanoparticle” based cells were fabricated from Dyesol 18NR-T paste which is composed

of ~ 20nm diameter 100% anatase nanoparticles, with a post $TiCl_4$ treated film porosity of approximately 58%, a surface area of 62 m^2/g and a pore size of 23nm as determined by nitrogen adsorption mesurments.

In **Figure 4b** the current voltage (JV) curves for the best performing devices of each paste recipe are shown, along with a standard nanoparticle based reference cell fabricated in the same series. The short-circuit current and overall performance improve with reduction of the titania content in the recipe. The titania1:3 device generated a very competitive short-circuit current of 7.5 $mAcm^{-2}$ and an overall efficiency of 3.2% measured under simulated AM1.5 sun light at $100mWcm^{-2}$. This is a 100% improvement upon our previous best reported block copolymer assembled solid-state DSC[18] where the assembly and crystalisation took place directly upon the FTO glass substrate, it is also extremely close to the standard nanoparticle based device,[35] which in our case delivered 3.4 % power conversion efficiency.

The primary reason for varying the composition of the metal-oxide precursor sol over a broad range was to systematically change the material structure and properties in order to improve our understanding of the critical factors which limit and improve device performance. TiO_2 synthesis via copolymer-directed self-assembly is a very different route compared to the traditional colloidal assembly, and hence broadens the scope for optimising TiO_2 properties for DSCs, and furthermore opens up the parameter space available for detailed investigation. In order to investigate differences in electronic behaviour between the various devices fabricated in this study, we have performed small perturbation transient photovoltage and photocurrent decay and collection measurements, see experimental section for details. These experiments allow us to derive the transport and recombination properties in the solar cells as well as the nature and distribution of sub band gap states within the titania films.

The diffusion coefficient (D_e) is estimated from the current collection lifetime (τ_{trans}) as $D_e = w^2/2.35\tau_{trans}$ where w is the film thickness.[36] In **Figure 5a** the diffusion coefficient versus incident light intensity is presented for devices incorporating the three titania compositions compared to a standard nanoparticle based solar cell. The diffusion coefficients increase weakly with light intensity, and are similar for all four devices, signifying similarly good charge transport in all compositions. For the solar cell to operate efficiently charges must be collected much faster than they recombine within the active layer. To estimate how far the charges travel at short-circuit before recombining, we estimate the charge lifetime (τ_e) in this regime by performing constant current transient photovoltage decay measurements at short-circuit. The electron diffusion length (L_D) can then be calculated as $L_D = \sqrt{D_e\tau_e}$. For the block copolymer derived devices the diffusion length drops slightly with increasing illumination intensity, and at the equivalent to full sun light intensity it is almost identical for the three titania recipes at about 3.5 μm. The diffusion lengths are lower at full sun intensity as compared to the standard nanoparticle based devices, but we estimate the current collection efficiency (η) at 100 mWcm^{-2} as $\eta = k_{trans}/(k_{trans} + k_{rec})$, where $k_{rec} = 1/\tau_e$, to be very similar for all devices at 94% for the titania 1:3, 97% for the titania 1:1, and 92% for the titania 2:1, as compared to 96 % for the standard cell. Since current collection efficiencies are close to unity for all optimised devices, the variations observed in photovoltaic performance must stem from another process than from inefficient charge collection.

For further investigation, we have used the current collection and voltage perturbation measurements to probe the location and density of the sub band gap states. In brief, we shine light onto the cell to generate a certain open-circuit voltage and then flash the cell with a further light pulse, generating a small voltage perturbation (ΔV) which is recorded.

The device is subsequently short-circuited, exposed to the same flash of light and the collected current is integrated to estimate the generated charge (ΔQ). Knowing both, the voltage perturbation (ΔV) and the total amount of charge which is generated by the light pulse (ΔQ), the chemical capacitance $C = \Delta Q/\Delta V$ at a given open-circuit voltage can be derived (see experimental section for further details). A schematic of the density-of-states (DOS) is shown in **Figure 5c**. **Figure 5d** shows the sub band gap density-of-states distribution, or chemical capacitance, extracted from these measurements. We observe a clear and significant trend between the titania synthesised in the three different ways. As the titania content is reduced, a deepening and a broadening of the DOS is observed. This systematic trend suggests that the crystallization environment strongly affects the electronic material properties of the copolymer directed titania. Titania films stemming from a network in which the inorganic component represents the majority phase (i.e. titania 2:1) lead to devices with fewer sub band gap states, or to sub band gap states that lie at higher energies. The more open monolith structures (titania 1:3, titania 1:1) lead to a deepening and broadening of the DOS distribution, which is most distinct when the crystallising inorganic component represents the minority phase for titania 1:3. In comparison to the diblock copolymer directed devices, the standard nanoparticle based cell has an even deeper and broader DOS distribution. We note that all mesoporous films were subject to a surface treatment with $TiCl_4$ prior to re-sintering, which grows a thin shell of titania upon the surface. This suggests that the changes to the density-of-states observed are not due to states residing directly upon the surface of the mesoprous material, due to the presence of the $TiCl_4$ grown titania shell. Nor are they due to a change in the interaction between the titania and the spiro-OMeTAD phases.

We attribute the fine-tuning of DOS distribution to the existence of the surrounding reducing organic component, which may be acting as an oxygen sink during calcination.

The density of sub band gap states in **Figure 5d** is most likely due to oxygen vacancies which increase with increasing the volume fraction of the polymer surrounding the amorphous titania during calcination. It is therefore intriguing to further study the interplay of sample composition, with annealing temperatures and atmosphere, to achieve full control over the sub band gap DOS. We further note that carbon contamination of the TiO_2 by the organic components, is an unlikely explanation for the observed results, given the increased efficiency of the devices with higher organic to inorganic ratio. Studies by Lee et al. have shown that the carbon content of the initially hybrid material is lost during the calcination process in an oxygen rich environment. [17]

To correlate device performance with the sub band gap DOS, we see a clear trend of increasing photocurrent and reducing open-circuit voltage with increasing the depth and width of the DOS: The open-circuit voltage is generated by the offset of the quasi-Fermi level for electrons in the TiO_2 with the quasi-Fermi level for holes in the spiro-OMeTAD (or hole polaron level). The shallower and narrower the DOS distribution, the lower (closer to vacuum) the quasi-Fermi level for electrons will be for any given photogenerated charge density. This is in line with our findings of increasing open circuit voltage from 0.77 V for the standard nanoparticle based cell over 0.82 V for titania 1:3 up to 0.90 V for titania 2:1, shown in **Figure 4b**. The increasing photocurrent with increasing the depth of the density of sub band gap states cannot be explained by considering transport and recombination, since these are remarkably unaffected by the titania synthesis. However, if we consider that photoinduced electron transfer from the dye to the titania is strongly influenced by the position and density of the sub band gap states,[37] then the observed trend of increasing photocurrent with increasing depth of the DOS distribution is justifiable. If electron transfer from the photoexcited dye into the TiO_2 is a tunnelling process, then increasing the density-of-states into which the electron

can be transferred would be expected to increase the rate and efficiency of electron transfer and charge generation. Since we observe increased photocurrent as the density of sub band gap states in the mesoporous titania is increased, this implies that a large fraction of the electrons are not injected into the conduction band, but directly into the sub band gap states. Koops *et al.* made a similar observation for the electron transfer from a ruthenium complex dye termed N719 into TiO_2 and conclude that intersystem crossing from the singlet to the triplet state competes with ultra-fast electron transfer into the TiO_2.[37] Due to the lower energy of the triplet state in the N719 dye, electron injection from this state has to proceed via the sub band gap states and is hence dependent upon the position and density of such states. Since an all organic dye is used in our study, intersystem crossing is unlikely to be fast. However, dye aggregation has also been observed to slow down electron transfer,[38] and the indolene based organic dyes used here are prone to aggregation,[39] and specifically for D102 J-aggregates are known to form which result in a significant deepening of the dye LUMO level. Furthermore, if dye aggregation occurs then the excited state may delocalise over one or more dye molecules, significantly reducing both the excited state energy of the electron and the "push-pull" orientation of the excited state, and hence increase the requirement for a large density of sub band gap states into which electron transfer can occur.

The intriguing result here is that by controlling the mesoscale morphology of the TiO_2 by diblock copolymer assisted self-assembly, it is possible to systematically vary the distribution of electronic sub band gap states in the material. Our study highlights the criticality of the energetic location and distribution of sub band gap states, and their role in efficient photocurrent generation in solid-state DSCs. We note that such an apparent control of the nature of the sub band gap states in mesoporous TiO_2 is not easily achievable through conventional colloidal synthesis routes.

3. Conclusions

In summary, we have synthesised mesoporous TiO_2 in different crystallization environments through the use of the diblock copolymer PI-*b*-PEO. The influence of the crystallization environment on the electronic properties of the materials and performance characteristics of solid-state DSCs incorporating the mesoporous TiO_2 was investigated. We find that the density and distribution of sub band gap states is a function of the synthesis conditions and critically affects the performance characteristics of self-assembled titania in hybrid solar cells. This gives us a new degree of freedom to vary and optimise towards the goal of controlling functional electronic hybrid interfaces. Specifically here, as the width and depth of the density of sub band gap states is increased, a significant enhancement in the photocurrent generation is observed. We postulate that this is due to the requirement for an abundance of sub band gap states into which efficient electron transfer can occur from the photoexcited sensitizers. Higher photocurrent generation is accompanied by an overall drop in open-circuit voltage with increasing density of sub band gap states, reflected in a trade-off in terms of the overall power conversion efficiency. These findings do not necessarily imply that a high density of sub band gap states are required in an ideal DSC, but rather serious losses in the charge generation mechanism take place. Reducing the heterogeneity and increasing the efficiency of this electron transfer and charge separation process are likely to be central goals for dramatic efficiency improvements in solid-state DSCs.

4. Experimental

Mesostructure fabrication:

3.45 mL of 37% HCl were rapidly added to 5 mL of titanium ethoxide in a beaker at 50

ºC under stirring. The resulting sol was left to age for 90 minutes. In a separate vial, 0.1 g of PI-*b*-PEO copolymer (M_n=33.5 kg/mol, polydispersity 1.03, 23 wt% PEO) was dissolved in 7 ml THF. The appropriate amount of the sol was added into the polymer solution to adjust the ratio of final (calcined) TiO_2 to added polymer by weight, to the three ratios 2:1, 1:1, and 1:3. For example, for titania 2:1, 0.873 ml sol was mixed with 0.1g PI-*b*-PEO in 7 ml THF. The solution was left to dry in air at 50 ºC. The dry material was then redissolved in a toluene and 1-butanol mixture where the ratio of the to solvents was adjusted to match the PI:(PEO+sol) weight fraction (for example for titania 2:1, the mixture consisted of 0.81 ml toluene and 0.61 ml 1-butanol). Finally, the solution was cast into a PTFE dish and left in air at 50°C for over 24 hours. The resulting material was heated slowly (5 ºC per minute) to 500 ºC, calcined for 1 hour at 500 ºC, and then left to cool down over 4 hours.

The powder was processed into a paste in a similar way as described by Ito *et al*.[27] (quantities quoted are for 1 g of TiO_2 powder). The TiO_2 powder was ground lightly in an alumina mortar for 10 seconds dry and for a further 1 second after the addition of 167 µl of acetic acid. 833 µl of deionised water was added and then the powder was ground for further 30 seconds. The paste was then transferred into a vial after adding 16 ml of ethanol. This solution was stirred with a magnetic stirrer for 1 minute and then sonicated with an ultrasonic probe 15 times with an interval of 2 seconds on, 2 seconds off. 3.33 g of α-terpineol was added and the paste was again stirred for 1 minute and then sonicated following the same procedure. Finally 5 g of a 10 weight-% solution of ethyl-cellulose (1:1, 10000cps:46000 cps) and ethanol were added, stirred and sonicated. The paste was then heated to 60 ºC for 24 h in air to evaporate the ethanol, and then redispersed in ethanol at a concentration of 1 ml ethanol per 1 g of paste, which was then further diluted down with ethanol to different concentrations to obtain a range of final film thicknesses.

Solar Cell assembly:

Fluorine doped tin oxide (FTO) coated glass sheets (15 Ω/□ Pilkington) were etched with zinc powder and HCl (2 Molar) to obtain the required electrode pattern. The sheets were then washed with soap (2% Hellmanex in water), de-ionized water, acetone, methanol and finally treated under an oxygen plasma for 10 minutes to remove the last traces of organic residues. The FTO sheets were subsequently coated with a compact layer of TiO_2 (100 nm) by aerosol spray pyrolysis deposition at 450 ºC, using air as the carrier gas. The meso-structured paste was then doctor bladed by hand (scotch tape and pipette) on the TiO_2 compact layer coated FTO sheets. The sheets were then slowly heated to 500 ºC (ramped over 1 ½ hours) and baked at this temperature for 30 minutes in air. After cooling, slides were cut down to size and soaked in a 20 mM $TiCl_4$ aqueous bath for 1 hour at 70 ºC in an incubator. After rinsing with deionised water and drying in air, the films were baked once more at 500 ºC for 45 min in air, then cooled down to 70 ºC and finally introduced in a dye solution for 1 hour. The indolene dye used was D102,[35] 0.2 mM in a 1:1 volume ratio of tert-butanol and acetonitrile. Spiro-OMeTAD was dissolved in chlorobenzene at varying concentrations ranging from 2.5 vol% to 35 vol%, and then heated up to 100º C. After fully dissolving the hole transporter, 4-*tert*-butyl pyridine (*t*BP) was added with a volume to mass ratio of 1:26 µl mg^{-1} *t*BP:spiro-OMeTAD. Lithium bis(trifluoromethylsulfonyl)imide salt (Li-TFSI) was pre-dissolved in acetonitrile at 170 $mg \cdot ml^{-1}$, then added to the hole transporter solution at 1:12 $\mu l \cdot mg^{-1}$ of Li-TFSI solution:Spiro-OMeTAD. When changing the hole transporter concentration, these two ratios were kept constant. The dyed films were rinsed briefly in acetonitrile and dried in air for 1 minute. Then a small quantity of the hole transporter solution 18-25 µl was dispensed onto each substrate and left to wet the films for 20 s before spin-coating at

2000 rpm for 25 s in air. The films were left for a minimum period of four hours in air before placing them in a thermal evaporator where 150 to 300 nm thick silver electrodes were deposited through a shadow mask under high vacuum (10^{-6} mbar). The active area of the devices was defined by a metal optical mask with 0.1256 cm^2 aperture.

For devices labelled "Standard", the substrates were prepared in the same way as the previous section. The mesoporous paste used was purchased from Dyesol (Dyesol 18NR-T) and it was diluted down with ethanol at a 3 ml per 1 g of paste ratio to obtain final thicknesses through doctor blading of 1.8 ± 0.1 μm. The devices were then subjected to the same sample preparation procedures as the block-copolymer derived structures.

Electron microscopy and x-ray characterisation:

TEM samples of the PI-*b*-PEO/TiO2 mesostructure were prepared by sectioning the bulk materials to 50nm with a Leica Ultracut UCT cryo-ultramicrotome and transferring the slices onto copper TEM grids. These samples were imaged in a Tecnai T12 Spirit TEM with an acceleration voltage of 120keV. Scanning electron microscopy of processed titania films and devices was carried out on a Leo Ultra 55 with a field emission source of 3 kV acceleration voltage.

SAXS patterns were recorded in the G1 beamline in Cornell High Energy Synchrotron Source (CHESS) with a Flicam 2D CCD detector, with the beam energy at 10.5 keV and the sample-to-detector of 2.3 m.

Wide-angle x-ray diffraction was carried out on a Bruker D8 diffractometer with a Kα beam of λ = 1.5406 Å. Spectra were taken with a step size of 0.00929° and a dwell time of 0.5 s/step.

Transient photocurrent and photovoltage decay technique:

Transient open circuit voltage decay measurements were performed by a similar method to O'Regan et al [40] and as described elsewhere[33]: a white light bias was generated from an array of diodes (Lumiled Model LXHL-NWE8 whitestar) with red light pulsed diodes (LXHLND98 redstar, 200 μs square pulse width, 100 ns rise and fall time) as the perturbation source, controlled by a fast solid-state switch. The voltage dynamics were measured on a 1GHz Agilent oscilloscope across the high impedance (1 MΩ) port. The perturbation light source was set to a suitably low level such that the voltage decay kinetics were monoexponential. This enabled the charge recombination rate constants to be obtained directly from the exponential decay rate of the voltage decay. Small perturbation transient photocurrent measurements were performed in a similar manner to the open-circuit voltage decay measurement. However, the signal was recorded directly through a low impedance port (50 Ω) on the oscilloscope, enabling short-circuit conditions. For the "voltage decay" measurements in the short-circuit regime, a Keithley 2400 sourcemeter was connected in series with the solar cell and parallel with the oscilloscope which was set on the high impedance port. The Keithley sourced the current through the solar cell which was under bias illumination in such a way that the voltage was kept at 0 V (i.e. short-circuit). In this way no extra current is allowed to flow through the device following the light pulse, therefore the decay of the measured perturbation signal is entirely governed by the charge recombination within the cell. For the current decay measurements, while the charge is being collected the charges are also simultaneously recombining within the cell. Therefore the decay rate constant for the current signal (k_{signal}) is a combination of the decay rate constant for the transport out of the cell (k_{trans}) and the rate constant for the recombination in the cell (k_{rec}) as, $k_{signal} = k_{trans} + k_{rec}$. In order to calculate the chemical capacitance (C) of the device, the total charge injected from the light pulse (ΔQ) is estimated from the integration of the area

under the measured current decay curve at short-circuit. The voltage perturbation (ΔV) is extracted from the peak of the voltage perturbation under open circuit conditions under the same bias light intensity. The capacitance is then calculated as $C = \Delta Q/\Delta V$.

Acknowledgements

This work was funded in part by by the EPSRC Nanotechnology Grand Challenges Energy grant (EP/F056702/1), and EP/F065884/1, the Department of Energy (DE-FG02 87ER45298) through the Cornell Fuel Cell Institute (CFCI), the National Science Foundation (DMR-0605856), and the Cornell Universiy KAUST Center for Research and Education. S.H. acknowledges a scholarship of the Bayerische Graduiertenförderung and funding from European RTN-6 Network "Polyfilm". We thank Natalie Plank for her assistance with the SEM, Mathias Kolle for the graphic design and Dominik Eder for the nitrogen sorption measurements and useful discussions, Frederic Sauvage from EPFL for information concerning the porosity and surface area of the standard Dyesol Paste and Hidetoshi Miura from Chemicrea inc. Japan for supplying the D102 sensitizer.

Received: ((will be filled in by the editorial staff))
Revised: ((will be filled in by the editorial staff))
Published online: ((will be filled in by the editorial staff))

[1] H. Gleiter, *Acta Mater.* **2000**, *48*, 1.
[2] J. Y. Ying, C. P. Mehnert, M. S. Wong, *Angew. Chem. Int. Ed.* **1999**, *38*, 56.
[3] P. T. Tanev, M. Chibwe, T. J. Pinnavaia, *Nature* **1994**, *368*, 321.
[4] M. A. Abkowitz, H. Antoniadis, J. S. Facci, S. A. Jenekhe, B. R. Hsieh, M. Stolka, *Molecular Crystals and Liquid Crystals Science and Technology Section a-Molecular Crystals and Liquid Crystals* **1994**, *252*, 1.
[5] S. Cosnier, C. Gondran, A. Senillou, M. Gratzel, N. Vlachopoulos, *Electroanalysis* **1997**, *9*, 1387.
[6] V. S. Y. Lin, K. Motesharei, K. P. S. Dancil, M. J. Sailor, M. R. Ghadiri, *Science* **1997**, *278*, 840.
[7] S. E. Gledhill, B. Scott, B. A. Gregg, *J. Mater. Res.* **2005**, *20*, 3167.
[8] C. B. Murray, C. R. Kagan, M. G. Bawendi, *Annual Review of Materials Science* **2000**, *30*, 545.
[9] C. T. Kresge, M. E. Leonowicz, W. J. Roth, J. C. Vartuli, J. S. Beck, *Nature* **1992**, *359*, 710.
[10] C. Park, J. Yoon, E. L. Thomas, *Polymer* **2003**, *44*, 6725.
[11] E. J. W. Crossland, M. Kamperman, M. Nedelcu, C. Ducati, U. Wiesner, D.-M. Smilgies, G. E. S. Toombes, M. A. Hillmyer, S. Ludwigs, U. Steiner, H. J. Snaith, *Nano Lett.* **2008**, *9*, 2807.
[12] E. J. W. Crossland, M. Nedelcu, C. Ducati, S. Ludwigs, M. A. Hillmyer, U. Steiner, H. J. Snaith, *Nano Lett.* **2009**, *9*, 2813.
[13] M. Templin, A. Franck, A. D. Chesne, H. Leist, Y. Zhang, R. Ulrich, V. SchÃ¤dler, U. Wiesner, *Science* **1997**, *278*, 1795.
[14] Y. L. K.M. Coakley, M.D. McGehee, K.L. Frindell, G.D. Stucky,, *Adv. Funct. Mater.* **2003**, *13*, 301.
[15] P. D. Yang, D. Y. Zhao, D. I. Margolese, B. F. Chmelka, G. D. Stucky, *Nature* **1998**, *396*, 152.
[16] D. Fattakhova-Rohlfing, M. Wark, T. Brezesinski, B. M. Smarsly, J. Rathousky, *Adv. Funct. Mater.* **2007**, *17*, 123.
[17] J. Lee, M. C. Orilall, S. C. Warren, M. Kamperman, F. J. Disalvo, U. Wiesner, *Nat. Mater.* **2008**, *7*, 222.
[18] M. Nedelcu, J. Lee, E. J. W. Crossland, S. C. Warren, M. C. Orilall, S. Guldin, S. Huttner, C. Ducati, D. Eder, U. Wiesner, U. Steiner, H. J. Snaith, *Soft matter* **2009**, *5*, 134.
[19] P. F. W. Simon, R. Ulrich, H. W. Spiess, U. Wiesner, *Chemistry of Materials* **2001**, *13*, 3464.
[20] B. Oregan, M. Gratzel, *Nature* **1991**, *353*, 737.
[21] J. M. Kroon, N. J. Bakker, H. J. P. Smit, P. Liska, K. R. Thampi, P. Wang, S. M. Zakeeruddin, M. Gratzel, A. Hinsch, S. Hore, U. Wurfel, R. Sastrawan, J. R. Durrant, E. Palomares, H. Pettersson, T. Gruszecki, J. Walter, K. Skupien, G. E. Tulloch, *Progress in photovoltaics* **2007**, *15*, 1.
[22] U. Bach, D. Lupo, P. Comte, J. E. Moser, F. Weissortel, J. Salbeck, H. Spreitzer, M. Gratzel, *Nature* **1998**, *395*, 583.
[23] H. J. Snaith, A. J. Moule, C. Klein, K. Meerholz, R. H. Friend, M. Gratzel, *Nano Lett.* **2007**, *7*, 3372.
[24] N. Kopidakis, N. R. Neale, K. Zhu, J. van de Lagemaat, A. J. Frank, *Appl. Phys. Lett.* **2005**, *87*.
[25] K. D. Benkstein, N. Kopidakis, J. van de Lagemaat, A. J. Frank, *J. Phys. Chem. B* **2003**, *107*, 7759.
[26] S. G. Mihaela Nedelcu, M. Christopher Orilall, Jinwoo Lee,, S. H. Scott C. Warren, Edward J. W. Crossland, Caterina Ducati,, D. E. Pete R. Laity, Ulrich Wiesner,, U. S. a. H. J. Snaith, *Chem. Mater.* **2009**, *[submitted]*.

[27] S. Ito, P. Chen, P. Comte, M. K. Nazeeruddin, P. Liska, P. Pechy, M. Gratzel, *Progress in photovoltaics* **2007**, *15*, 603.
[28] A density of 2 gcm^{-3} for the TiO_2 sol within the polymer can be estimated which results in a hydrophilic volume fraction of: 0.62 for 2:1, 0.49 for 1:1 and 0.3 for 1:3 ratios; corresponding to the expected diblock copolymer phase diagrams shown in Fig. 1 b-d.
[29] E. L. Crepaldi, G. Soler-Illia, D. Grosso, F. Cagnol, F. Ribot, C. Sanchez, *Journal of the American Chemical Society* **2003**, *125*, 9770.
[30] B. C. Garcia, M. Kamperman, R. Ulrich, A. Jain, S. M. Gruner, U. Wiesner, *Chemistry of Materials* **2009**, *21*, 5397.
[31] H. Y. Huang, Z. J. Hu, Y. Z. Chen, F. J. Zhang, Y. M. Gong, T. B. He, C. Wu, *Macromolecules* **2004**, *37*, 6523.
[32] F. Fabregat-Santiago, J. Bisquert, L. Cevey, P. Chen, M. K. Wang, S. M. Zakeeruddin, M. Gratzel, *J. Am. Chem. Soc.* **2009**, *131*, 558.
[33] H. J. Snaith, R. Humphrybaker, P. Chen, I. Cesar, M. Graetzel, *Nanotechnology* **2008**, *19*, 424003.
[34] I. K. Ding, N. Tetreault, J. Brillet, B. E. Hardin, E. H. Smith, S. J. Rosenthal, F. Sauvage, M. Gratzel, M. D. McGehee, *Adv. Func. Matter.* **2009**, *19*, 2431.
[35] L. Schmidt-Mende, U. Bach, R. Humphry-Baker, T. Horiuchi, H. Miura, S. Ito, S. Uchida, M. Gratzel, *Adv. Matter.* **2005**, *17*, 813.
[36] J. van de Lagemaat, A. J. Frank, *Journal of Physical Chemistry B* **2001**, *105*, 11194.
[37] S. Koops, B. O'Regan, P. R. F. Barnes, J. R. Durrant, *J. Am. Chem. Soc* **2009**, *131*, 4808.
[38] B. Wenger, M. Gratzel, J. E. Moser, *J. Am. Chem. Soc* **2005**, *127*, 12150.
[39] H. J. Snaith, A. Petrozza, S. Ito, H. Miura, M. Gratzel, *Adv. Funct. Mater.* **2009**, *19*, 1810.
[40] B. C. O'Regan, F. Lenzmann, *J. Phys. Chem. B.* **2004**, *108*, 4342.

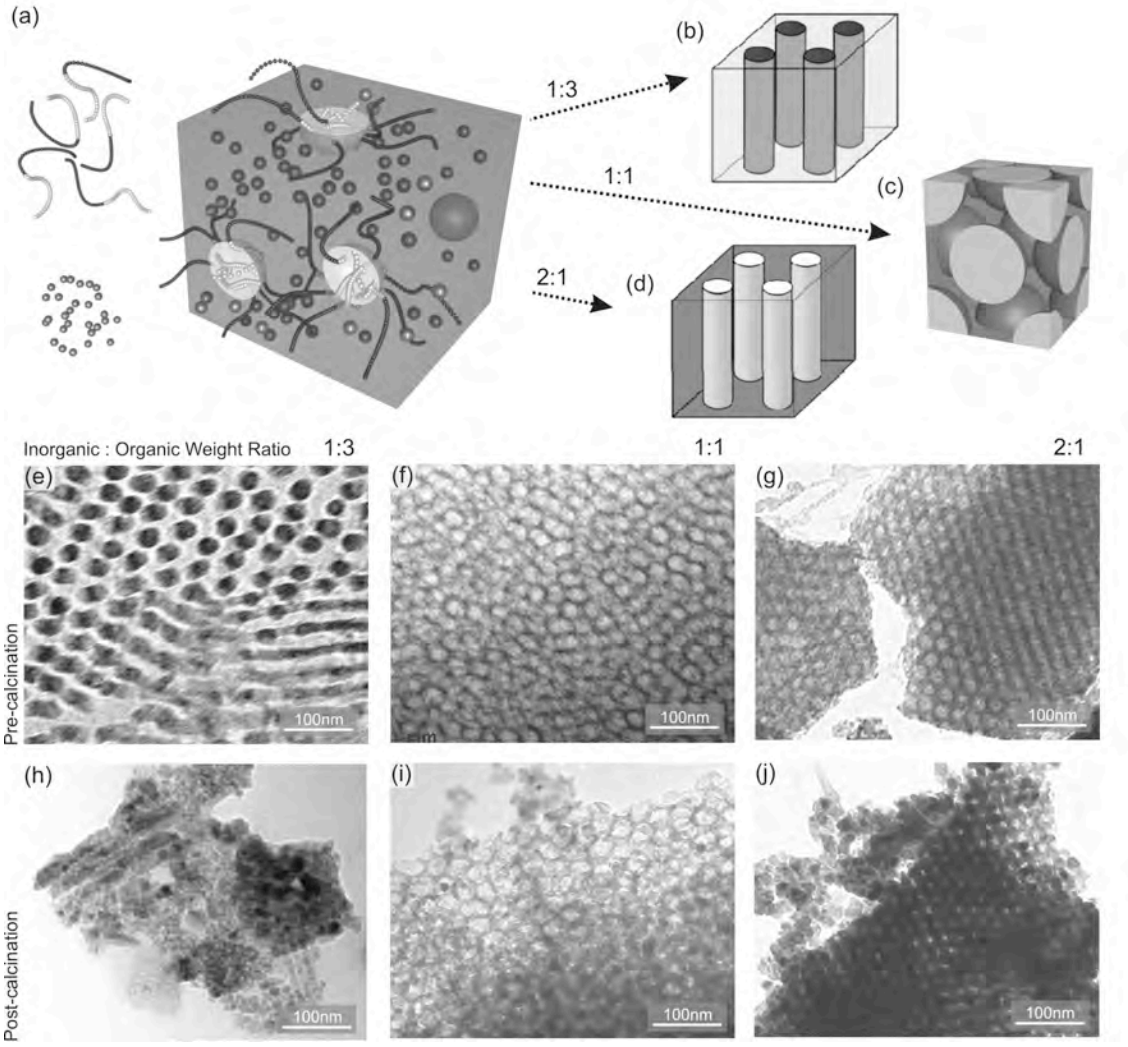

Figure 1. Morphologies of block copolymer directed titania before paste-processing. (a) Schematic drawing of the self-assembly process of TiO_2 within the block copolymer. Sol-particles are shown as small dark grey spheres, the PEO domains as dark grey chains and the PI phase is representend as light grey chains. The TiO_2 sol particles are shown to predominantly reside within the PEO phase. Different morphologies are obtained, depending on the titania load: (b) TiO_2 rich cylinders in an organic matrix for titania 1:3, (c) organic micelles in the TiO_2 rich matrix for titania 1:1 and (d) organic cylinders in a TiO_2 rich matrix for titania 3:1. (e) to (g) are bright field TEM images of the materials for the different recipes before calcination, i.e. as hybrid material. Light areas in (b)-(g) show the organic-rich domains and the dark areas correspond to the TiO_2 rich domains. (h) to (j) are TEM images of the calcined material for all three recipes (heated to 500 ºC in air).

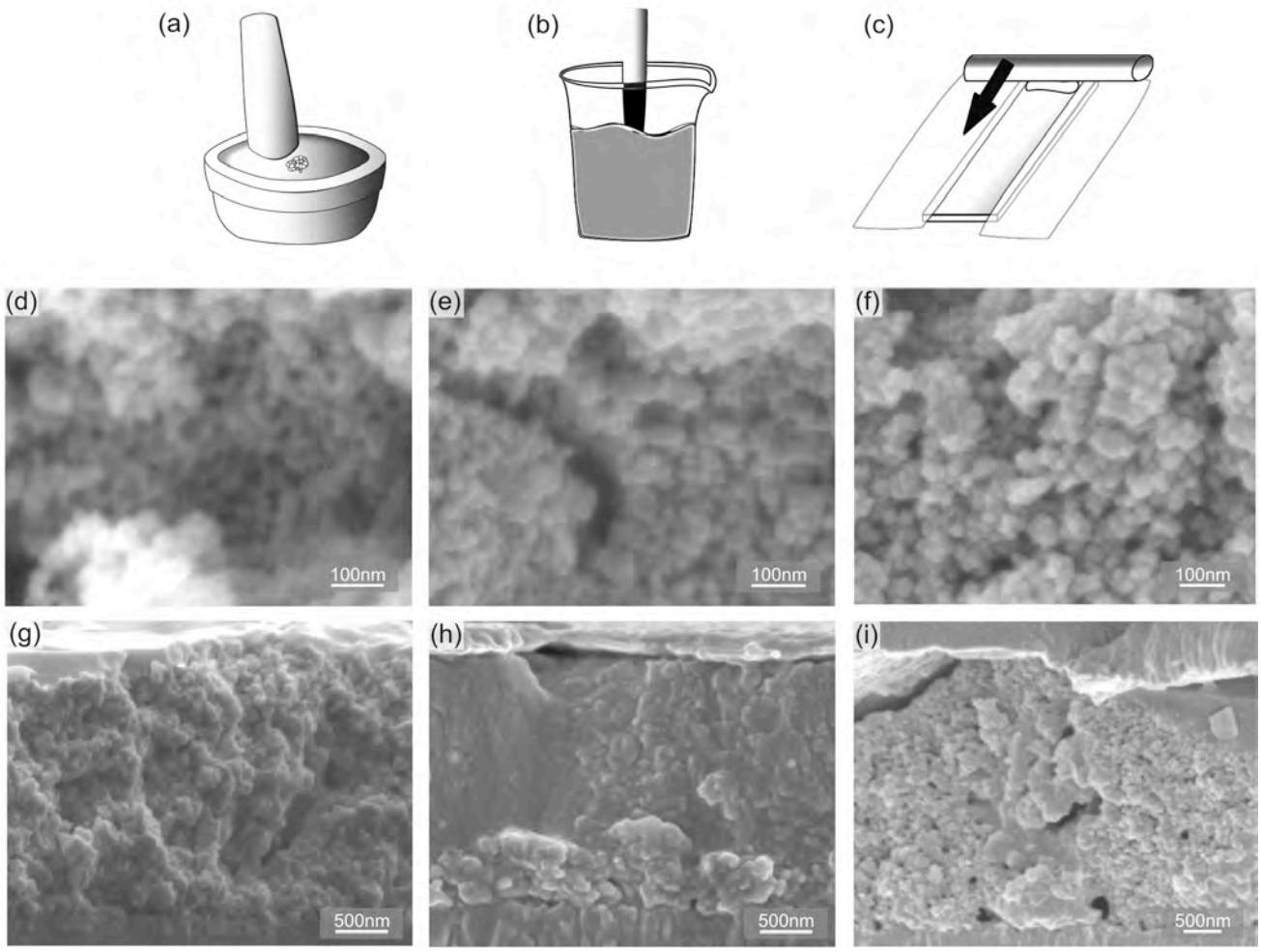

Figure 2. SEM images of the TiO_2 paste. (a) to (c) show the different steps in the paste reconstitution proces. First the annealed powder is lightly ground for 2 minutes (a), then cellulose and α-terpineol are added and the resulting mixture is sonicated (b), and finally the paste is doctor bladed to obtain thin films of around 2 μm in thickness (c). (d) to (f) are SEM surface images of the ensuing mesoporous TiO_2 after sintering the paste on the device substrates, (f) corresponds to titania 2:1, (e) to titania 1:1 and (d) to titania 1:3. (g) to (i) are the corresponding SEM images of device cross-sections.

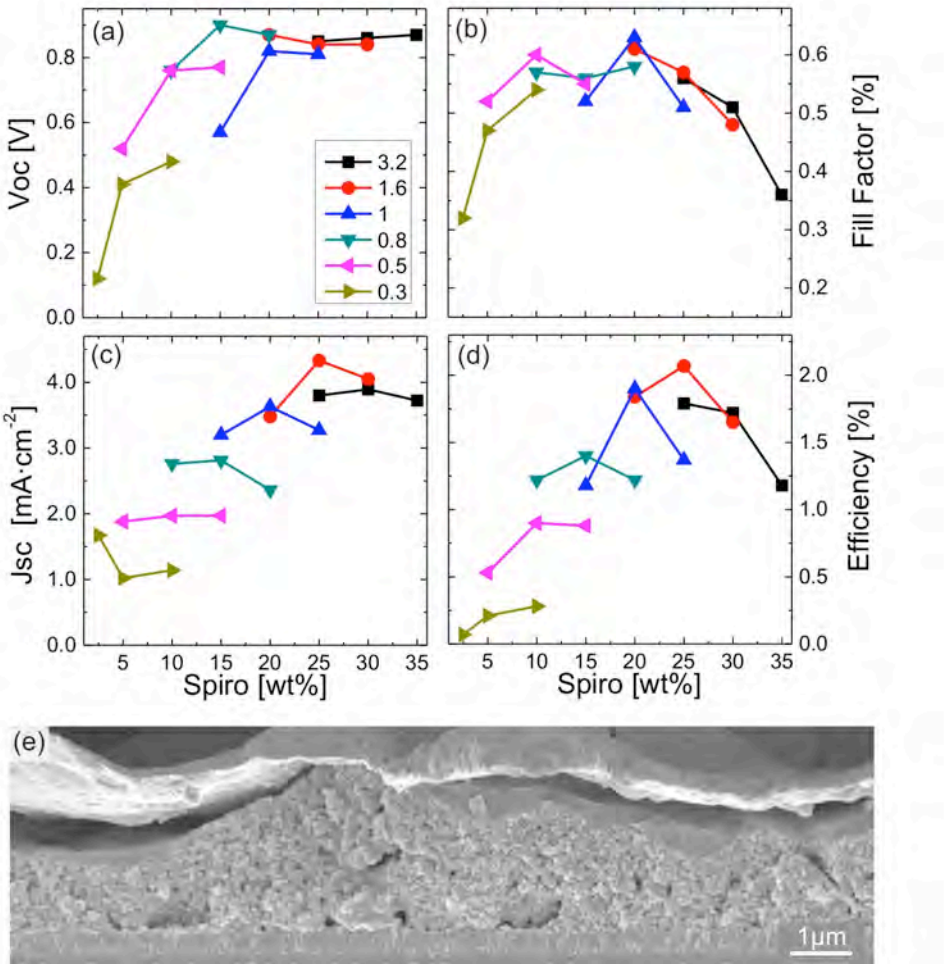

Figure 3. Pore filling optimisation. Graphs a to d show the solar cell performance parameters measured under full sun illumination for the titania 2:1 devices, where the numbers in the legend correspond to the film thicknesses in μm. Each data point is the result of the average from 3 to 6 devices. (a) Open-circuit voltage, (b) fill factor, (c) short circuit current and (d) power conversion efficiency. Error bars are omitted for clarity, but they are between 5-10% of the values shown. (e) A long cross-section of the optimized titania 1:3 device where the thickness varies between 1 and 3 μm.

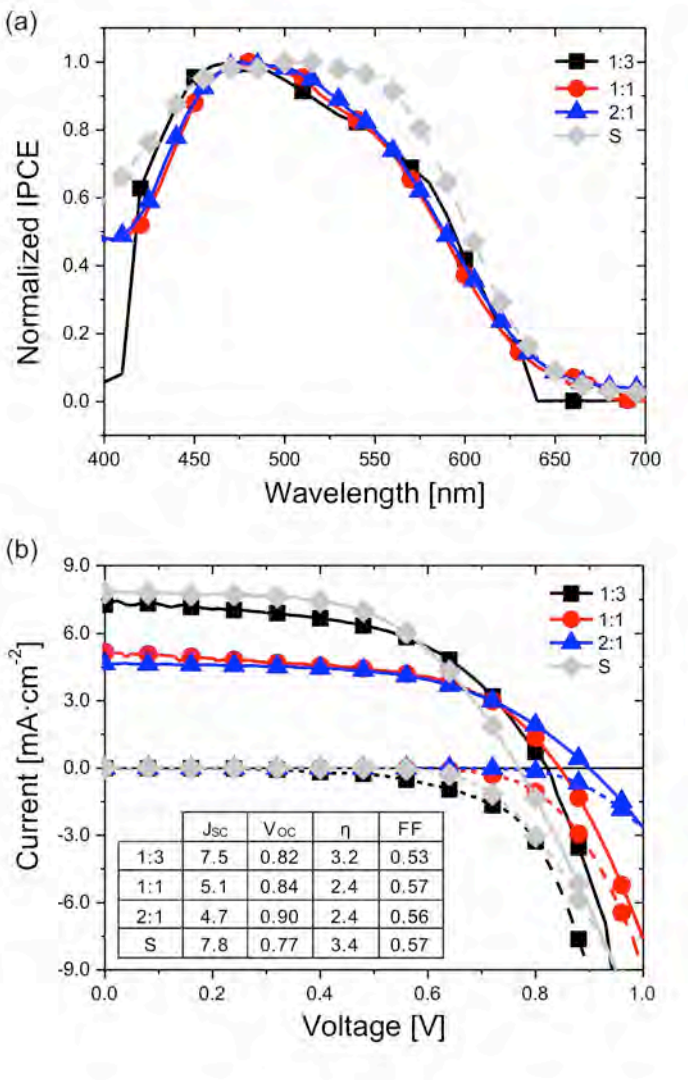

	Jsc	Voc	η	FF
1:3	7.5	0.82	3.2	0.53
1:1	5.1	0.84	2.4	0.57
2:1	4.7	0.90	2.4	0.56
S	7.8	0.77	3.4	0.57

Figure 4. a) Normalized incident photon-to-current conversion efficiency (IPCE) and b) current density-voltage (JV) curves of devices made from the 3 titania reipes (see legend). A reference device fabricated from a standard nanoparticle paste is shown as grey diamonds (S in the legend). Inset in b) shows the extracted values for the short-circuit current (Jsc), open-circuit voltage (Voc), power conversion efficiency (η) and fill factor (FF) for the 4 devices.

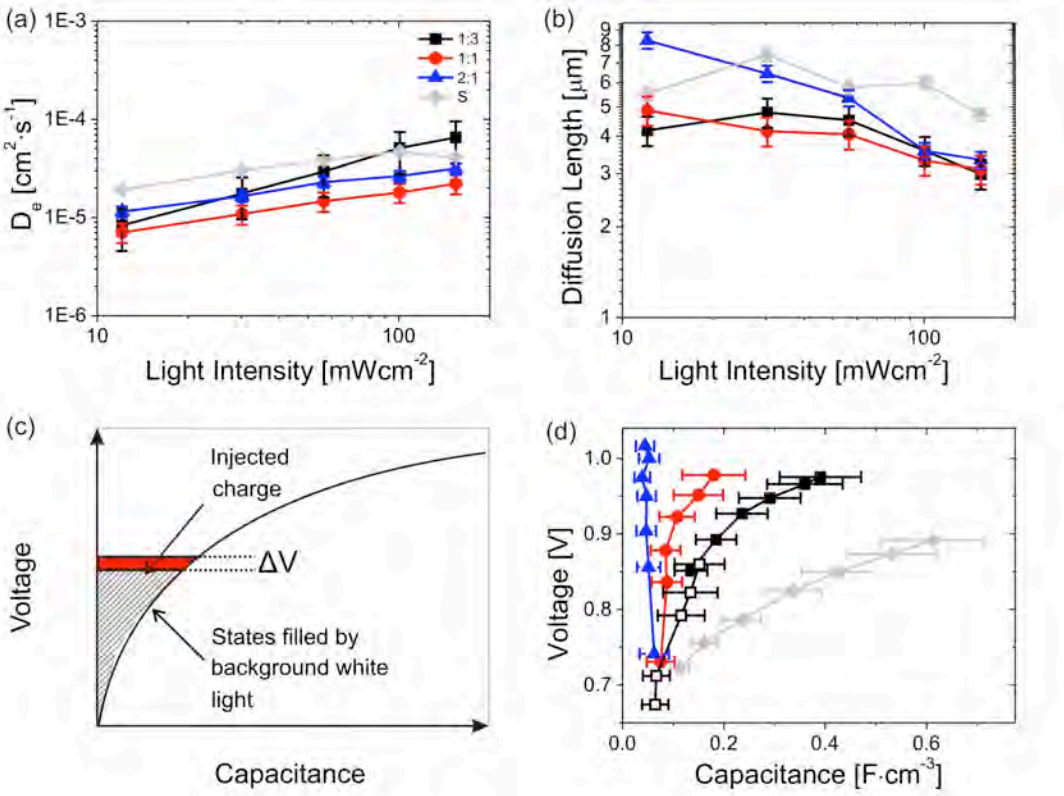

Figure 5. Transient photocurrent and photovoltage decay measurements. a) Diffusion coefficients (D_e) and b) diffusion lengths (L_D) extracted from transient photocurrent and photovoltage decay measurements plotted against different background white light intensities for the different titania recipes (see legend). A device made from standard (S) nanoparticle paste (diamonds) is also shown for comparison. c) Schematic diagram of the sub band gap density-of-states, plotted as voltage against capacitance. This shows persistantly filled states (shaded grey in diagonal stripes), which are populated by photo induced electron transfer from the background white light. Also shown in solid-red are states transiently filled from the red light pulse, which induce a small voltage purturbation. d) Data showing open-circuit voltage versus capacitance (calculated as $C = \Delta Q/\Delta V$ (injected charge/voltage purturbation)) where for titania 1:3, two cells of different thickness, 2 μm (open centre), and 0.8 μm (solid centre) are shown. Error bars in panels (a) and (b) are a result of the measurement errors and are dominated by the roughness of the films. Error bars in panel (d) are set at 10% of the value shown since multiple measurements on a single device yield this degree of variation. The data shown in this figure are from measurements on the same devices for which we present the current voltage curves in Figure 4b.

The table of contents entry

Titania synthesis via block copolymer self assembly is shown to control, not only morphological aspects, but also the electronic structure of TiO_2. This synthesis approach enables unparalleled tuning of operational functionality, when integrated into solid-state dye-sensitized solar cell. Peak power conversion efficiencies of 3.2% for thin solid-state dye-sensitized solar cells represents a doubling of the previous best efficiency for block-copolymer structured hybrid solar cells.

Keyword: self-assembly, pi-b-peo, block copolymer, dye-sensitizedsolar cell, solid-state

Pablo Docampo,[†] Stefan Guldin,[†] Morgan Stefik, Priti Tiwana, M. Christopher Orilall, Sven Hüttner, Ulrich Wiesner, Ulrich Steiner, and Henry J. Snaith*

Control of solid-state dye-sensitized solar performance by block copolymer directed TiO_2 synthesis

ToC figure ((Please choose one size: 55 mm broad × 50 mm high **or** 110 mm broad × 20 mm high. Please do not use any other dimensions))

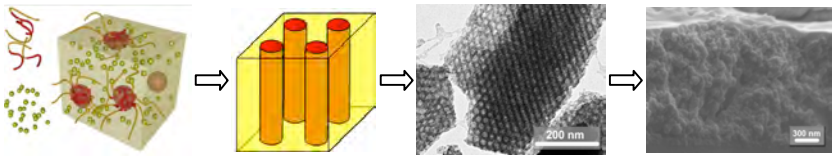

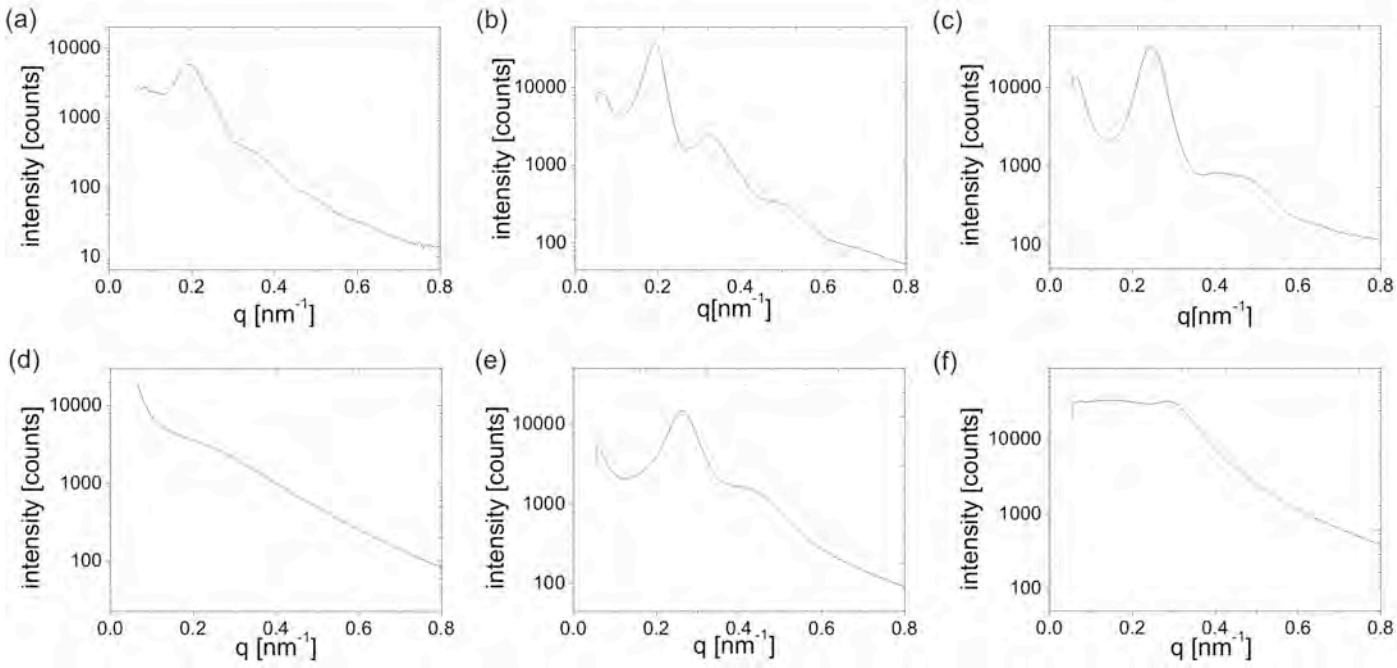

Supporting Material 1. Radially-integrated plots from small angle X-ray scattering patterns. The scattering vector, q, is defined as $q=4\pi\sin\theta/\lambda$, where θ is the scattering angle and λ is the x-ray wavelength. Plots (a) to (c) correspond to the pre-calcined hybrid samples of titania 1:3, 1:1, and 2:1, respectively. Plots (d) to (f) correspond to the calcined samples of titania 1:3, 1:1, and 2:1, respectively. Dotted lines in (a) and (c) show predicted peak positions for hexagonal morphologies calculated from the first reflection peak positions. Dotted lines in (e) are reminiscent with a micellar arrangement of pores as described in the text for the calcined titania 1:1 sample.

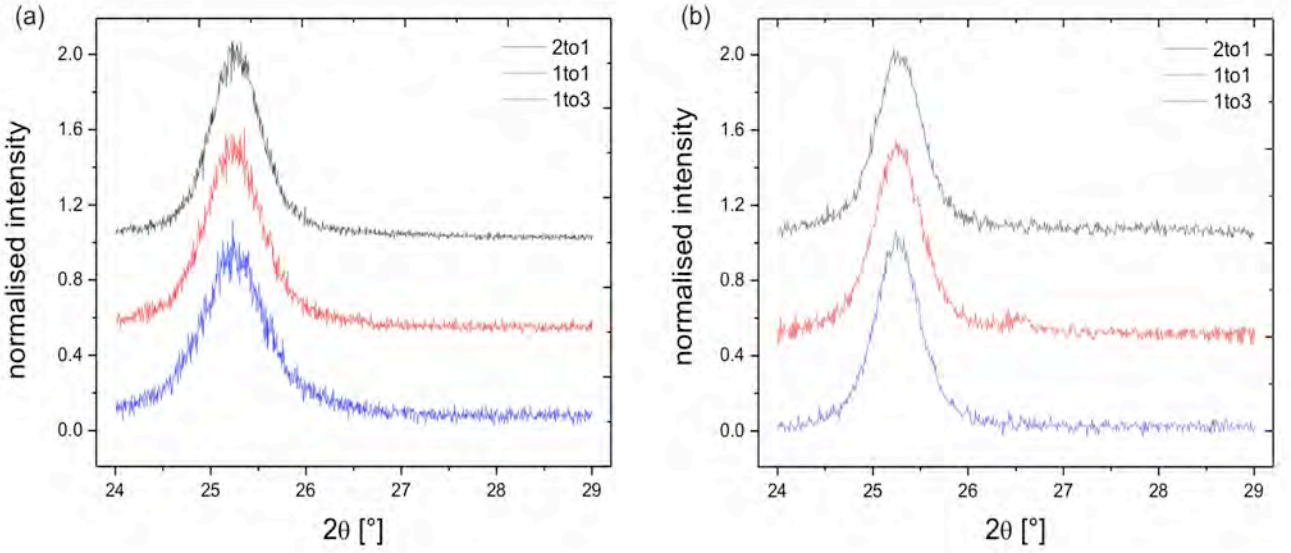

Supporting Material 2. Wide-angle X-ray scattering of calcined titania (a) before and (b) after paste processing. For better comparison between titania 2:1 (top), titania 1:1 (middle) and titania 1:3 intensities were normalized. Crystal sizes of the materials were determined by fitting the anatase (101) peak with a Voigt function and subsequently correlating the peak broadening to nanocrystallinity via the Debye-Scherrer equation with a K value of 0.89.

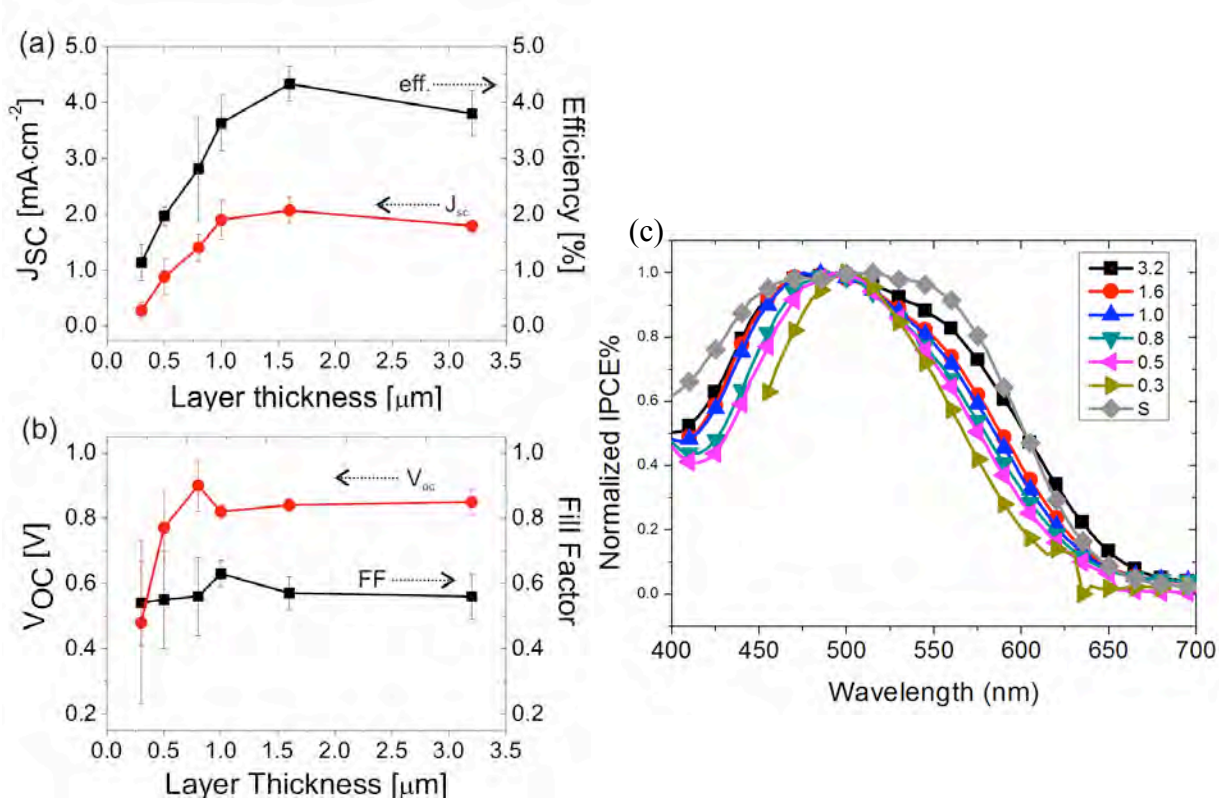

Supporting Material 3. Thickness dependence of devices incorporating the titania 2:1 morphology, parameters extracted from measurements of solid-state DSC with optimised hole transporter concentrations. a-b) Solar simulator parameters, where in a) efficiency (circles) and short-circuit current (Jsc, squares), and in b) open-circuit voltage (Voc, squares) and fill factor (circles), are all plotted against mesoporous layer thickness. Values shown are the average of 3 to 6 devices. c) Normalized incident photon-to-electron conversion efficiencies (IPCE) for the different mesoporous layer thicknesses plotted against wavelength. A 'standard' (S) nanoparticle device (diamonds) is shown for comparison.